

Sonochemical effects on single-bubble sonoluminescence

Li Yuan*

LSEC and Institute of Computational Mathematics,

Academy of Mathematics and Systems Science,

Chinese Academy of Sciences, Beijing 100080, People's Republic of China

(Dated: August 21, 2017)

Abstract

A refined hydrochemical model for single-bubble sonoluminescence (SBSL) is presented. The processes of water vapor evaporation and condensation, mass diffusion, and chemical reactions are taken into account. Numerical simulations of Xe-, Ar- and He-filled bubbles are carried out. The results show that the trapped water vapor in conjunction with its endothermic chemical reactions significantly reduces the temperature within the bubble so that the degrees of ionization are generally very low. The chemical radicals generated from water vapor are shown to play an increasingly important role in the light emission from Xe to He bubbles. Light spectra and pulses are then computed from an optically thin model. It is found that the resulting spectrum intensities are too small and the pulse widths are too short to fit to recent experimental results within stable SBSL range. Addition of a finite-size blackbody core to the optically thin model improves the fitting. Suggestions on how to reconcile the conflict are given.

PACS numbers: 78.60.Mq, 47.40.Fw, 43.25.+y

*Electronic address: lyuan@lsec.cc.ac.cn

I. INTRODUCTION

The discovery that acoustic energy can be converted to light through an oscillating air bubble trapped in water [1] has triggered extensive studies on single-bubble sonoluminescence (SBSL) (see reviews in Refs. [2, 3]). Under certain conditions, a stable and regular flash of blue-white light with a width of about 40–350 ps is emitted during the violent collapse of the bubble in each acoustic cycle [4, 5, 6]. Among many candidate mechanisms of SBSL light emission, the model that identified SBSL light emission as thermal bremsstrahlung and recombination radiation from an optically thin bubble seemed to predict the widths, shapes, and spectra of the emitted light fairly well under certain simplified hydrodynamic frameworks [7, 8, 9, 10]. Similar models included those which used finite opacity to define a variable blackbody core [11, 12, 13, 14, 15], whose suitability was reflected in the good fitting by a smaller-than-bubble blackbody [16]. However, different approximations in modelling the physical-chemical processes, and particularly, uncertainties under the extreme conditions inside a sonoluminescing bubble, may give diverse predictions that plague the validity of a light emission model. Therefore, more realistic hydrodynamic-chemical modelling and more critical tests of the light emission models under the refined hydro-chemical framework are necessary.

Past studies delineated the important effects of diffusive transport, surface tension, and compressibility of the surrounding liquid on SBSL [17, 18, 19]. Earlier studies [20, 21] considered the influence of evaporation-condensation phenomena on the bubble dynamics. Sochard *et al.* [22] and Gong *et al.* [23] coupled the bubble dynamics with the water vapor dissociations. Recently, the study of sonochemistry was extended from lower temperature to higher temperature situations where SBSL emerges [24, 25]. Yasui [24] presented a model of SBSL that accounts for evaporation-condensation process at the bubble interface and water vapor chemical reactions. It was later stressed by Storey and Szeri [26] and others [12, 27, 28, 29] that water vapor reduce the temperatures inside the SL bubble significantly by reducing the compression heating of the mixture and through primarily endothermic chemical reactions. In some of these models, spatial uniformity of the bubble interior was assumed and inter-molecular mass diffusion was not properly accounted for. As a consequence, such models tended to underpredict the amount of trapped water vapor during the rapid collapse.

In the full hydrochemical numerical study by Storey and Szeri [26], the consequences of water vapor inside strongly forced argon bubbles were investigated in detail. The interaction of nonlinearity of the volume oscillations, mass diffusion, and nonequilibrium phase change at the bubble wall resulted in excess water vapor trapped in the bubble during the violent collapse. The amount of trapped water vapor was more than that predicted by the simple model [24]. Akhatov *et al.* [30] accounted for the occurrence of supercritical conditions of condensation and studied laser-induced cavitation bubbles. The effects of water vapor diffusion in different noble gas bubbles were studied by Xu *et al.* [31], where shock waves were found to occur only in Xe bubbles. More recently, Toegel *et al.* [28] studied the effects of the highly compressed conditions of SL bubbles on chemical equilibrium constants. They showed that high temperatures could be recovered due to the suppressed water vapor dissociations. In spite of the progress made, the direct consequence of sonochemistry on existing popular light emission models is to be revealed in a full hydrodynamic model.

In this paper, we present a refined hydrodynamic model taking into account the chemical reactions and ionizations of the noble gas and water vapor mixture. The model is an extension of our previous ones [14, 15, 18]. As done for a pure argon bubble [15], the Navier-Stokes (NS) equations for the multispecies gas mixture in the bubble interior are coupled with a proper form of the Rayleigh-Plesset (RP) equation for the bubble wall, including the effects of liquid compressibility and heat transfer. The newly added feature is that the nonequilibrium processes of evaporation and condensation, species diffusion, noble gas exchange between the bubble and the surrounding liquid, and dissociations of water vapor and ionizations of atomic species inside the bubble are all taken into account. The numerical scheme for solving the hydrodynamic equations is modified to be a semi-implicit one which allows for better numerical stability than original explicit scheme in Ref. [18].

Detailed formulae in Eulerian framework are given. Numerical simulations are carried out for bubbles of He, Ar, or Xe gases. The effects of sonochemistry on current light-emitting models of SBSL [8, 12, 15] are studied in detail through comparison with a calibrated experiment [16]. The main conclusions are: (i) the chemical reactions reduce the temperature within the bubble to such an extent that the degrees of ionization are generally very low; (ii) shock waves do not appear in He or Ar bubbles in the stable SBSL regime, but can occur in Xe bubbles only at higher driving pressures; (iii) chemical radicals generated from the water vapor contribute dominantly to the light emission of He bubbles; (iv) based on the

computed photon absorption coefficients, the light spectra and pulse widths computed from the popular optically thin model can hardly be fitted to the experimental ones. Addition of a dynamic blackbody core to the optically thin model improves the fitting. Some suggestions on how to improve the optically thin model are outlined.

II. HYDRODYNAMIC MODEL

In this section, we extend our previous hydrodynamic model [15, 18] to include processes of evaporation and condensation on the wall and chemical reactions inside the bubble. The bubble is assumed to be spherically symmetric and is composed of the mixture of noble gas, water vapor, and reaction products. In addition to the NS and RP equations, the equations for the mass concentration of the dissolved noble gas and for the temperature of the surrounding water are also solved.

A. Gas dynamics in the bubble

1. The NS equations

The bubble is assumed to contain N -species gas mixture. Nonequilibrium chemical reactions of the water vapor and ionizations of the monatomic species (Ar, H, and O) are considered. The maximum ionization level is taken as 3 for a noble gas, and 1 for H or O atom. For an Ar bubble, $N = 13$: Ar, Ar⁺, Ar²⁺, Ar³⁺, H₂O, OH, H, H⁺, O, O⁺, H₂, O₂, e⁻. The dynamics inside the bubble is described by the compressible NS equations, which represent the conservation of mass, momentum and energy. They can be written into a “conservative” form in the spherical coordinates

$$\frac{\partial \mathbf{Q}}{\partial t} + \frac{\partial \mathbf{F}}{\partial r} = \mathbf{H} + \frac{1}{r^2} \frac{\partial r^2 \mathbf{F}_\nu}{\partial r} + \mathbf{M}_\nu + \mathbf{S}, \quad (1)$$

with

$$\mathbf{Q} = \begin{bmatrix} \rho_1 \\ \vdots \\ \rho_N \\ \rho u \\ \rho E \end{bmatrix}, \quad \mathbf{F} = \begin{bmatrix} \rho_1 u \\ \vdots \\ \rho_N u \\ \rho u^2 + P \\ u(\rho E + P) \end{bmatrix}, \quad \mathbf{H} = -\frac{2u}{r} \begin{bmatrix} \rho_1 \\ \vdots \\ \rho_N \\ \rho u \\ \rho E + P \end{bmatrix},$$

$$\mathbf{F}_\nu = \begin{bmatrix} -J_1 \\ \vdots \\ -J_N \\ \tau_{rr} \\ u\tau_{rr} + q \end{bmatrix}, \quad \mathbf{M}_\nu = \begin{bmatrix} 0 \\ \vdots \\ 0 \\ -(\tau_{\theta\theta} + \tau_{\phi\phi})/r \\ 0 \end{bmatrix}, \quad \mathbf{S} = \begin{bmatrix} \dot{\omega}_1 \\ \vdots \\ \dot{\omega}_N \\ 0 \\ 0 \end{bmatrix}, \quad (2)$$

and

$$\rho = \sum_{i=1}^N \rho_i, \quad E = e + \frac{u^2}{2}, \quad e = \sum_{i=1}^N e_i, \quad \tau_{rr} = -2\tau_{\theta\theta} = -2\tau_{\phi\phi} = \frac{4\mu}{3} \left(\frac{\partial u}{\partial r} - \frac{u}{r} \right),$$

$$q = \lambda \frac{\partial T}{\partial r} - \sum_{i=1}^N J_i h_i, \quad J_i = -\rho D_i^M \frac{M_i}{\bar{M}} \left[\frac{\partial X_i}{\partial r} + (X_i - Y_i) \frac{\partial \ln P}{\partial r} + K_i^T \frac{\partial \ln T}{\partial r} \right], \quad (3)$$

$$Y_i = \frac{\rho_i}{\rho}, \quad X_i = Y_i \frac{\bar{M}}{M_i}, \quad \bar{M} = \frac{1}{\sum_{i=1}^N \frac{Y_i}{M_i}}, \quad D_i^M = \frac{1 - Y_i}{\sum_{j \neq i}^N X_j / D_{ij}}, \quad h_i = e_i + \frac{P_i}{\rho_i},$$

where ρ_i is density of species i , ρ is the total density of gas mixture, P is the pressure, T is the temperature, u is the mass averaged velocity, e is the total internal energy of the mixture, e_i and h_i are the internal energy and enthalpy of species i , respectively, P_i is the partial pressure, μ and λ are the viscosity and the thermal conductivity of the mixture, respectively, Y_i and X_i are the mass fraction and mole fraction of species i , respectively, M_i is the molar mass of species i , \bar{M} is the mean molar mass of the mixture, D_{ij} is the binary diffusion coefficient between species i and j , D_i^M is the mean diffusion coefficient of species i into the mixture, K_i^T is the thermal diffusion ratio, τ_{rr} is the normal stress, J_i is the mass diffusion flux that must satisfy $\sum_{i=1}^N J_i = 0$, and $\dot{\omega}_i$ is the net mass production rate due to chemical reactions and ionizations that satisfies $\sum_{i=1}^N \dot{\omega}_i = 0$. Use of the mean diffusion coefficient is a practical approximation for computational efficiency [26, 32]. However, to ensure global mass conservation, a correction diffusion flux $J_i^c = \rho_i \sum_{i=1}^N D_i^M \frac{M_i}{\bar{M}} \left[\frac{\partial X_i}{\partial r} + (X_i - Y_i) \frac{\partial \ln P}{\partial r} + K_i^T \frac{\partial \ln T}{\partial r} \right]$ is added to J_i in Eq.(3), as recommended by Ref. [32]. It can be easily shown that the modified J_i satisfies $\sum_{i=1}^N J_i = 0$.

2. Transport properties, equation of state and thermodynamic properties

The individual transport properties (viscosity μ_i , thermal conductivity λ_i , thermal diffusion ratio k_i^T , and binary diffusion coefficient D_{ij}) are generally calculated based on

Chapman-Enskog theory [33, 34, 35]. However, the transport properties of the gas mixture, μ, λ are determined by some empirical combination rules such as Wilke's semiempirical formula [34]. There is also difficulty in describing individual μ_i and D_{ij} for some reaction products due to lack of data. We shall let unavailable μ_i and D_{ij} equal to other known ones, e.g., $\mu_{\text{OH}} = \mu_{\text{H}_2\text{O}}, \mu_{\text{H}} = \mu_{\text{H}_2}$. Collision cross sections of ions, electron, and some radical species that are not available in Ref. [33, 34] can be determined using NASA temperature-dependent polynomial fitting [36]. Once μ_i is known, λ_i is obtained by modified Eucken model [33, 34]. The trouble lies in the determination of k_i^T . In this regard, we only take into account the thermal diffusion between the noble gas and the water vapor, since thermal diffusion is only important in slow stage other than during collapse [26, 35]. The high pressure corrections [34] are applied to μ_i and λ_i similar to what Xu [31] did. The transport properties of the mixture μ and λ are obtained by using Wilke's semiempirical formula

$$\mu = \sum_{i=1}^N \left(\frac{X_i \mu_i}{\sum_{j=1}^N X_j \phi_{ij}} \right), \quad (4)$$

$$\lambda = \sum_{i=1}^N \left(\frac{X_i \lambda_i}{\sum_{j=1}^N X_j \phi_{ij}} \right), \quad (5)$$

where

$$\phi_{ij} = \left[1 + \left(\frac{\mu_i}{\mu_j} \right)^{1/2} \left(\frac{M_j}{M_i} \right)^{1/4} \right]^2 \left[\sqrt{8} \left(1 + \frac{M_i}{M_j} \right)^{1/2} \right]^{-1}. \quad (6)$$

The hydrodynamics of the bubble is affected by the equation of state. Here the gas mixture is modeled by a hardcore van der Waals equation of state that has the excluded volume but ignores the van der Waals force as the previous authors did [37]

$$P = \sum_{i=1}^N P_i = \frac{\rho R T}{1 - b \rho} = P(T, \rho_1, \dots, \rho_N), \quad (7)$$

where $R = \sum_{i=1}^N Y_i R_i, R_i = R_u / M_i$, R_u is the universal gas constant, $b = \sum_{i=1}^N Y_i b_i$ is a simple combination of b_i , with b_i being the van der Waals excluded volume in m^3/kg . The values of $\tilde{b}_i = b_i M_i$ (in cm^3/mol) are computed by $\tilde{b} = R T_c / 8 P_c$ where T_c and P_c are critical temperature and pressure of a species [34]. When these critical parameters are not available, b_i is taken as 4 times the spherical volume of the atomic or ionic radius.

A well-posedness of equation closure requires $P = f(e, \rho_1, \dots, \rho_N)$, therefore, T must be

solved for from the given energy relation

$$E = e + \frac{u^2}{2}, \quad e = \sum_{i=1}^N Y_i (C_{Vi} R_i T + e_i^0) + \sum_{i=\text{molecules}} Y_i e_i^V + \sum_{i=\text{ions}} Y_i e_i^I, \quad (8)$$

where the internal energy is divided into the translational and rotational, the vibrational, and the ionization parts. The coefficient of specific heat at constant volume C_{Vi} , is approximately assumed as follows [24]: $C_{Vi} = \frac{3}{2}$ for monatomic gases such as Ar, Ar⁺, H, O; $C_{Vi} = \frac{5}{2}$ for diatomic gases such as OH, H₂, O₂, and $C_{Vi} = \frac{6}{2}$ for other gases. e_i^0 is the reference energy, e_i^V is the vibrational energy of molecules species, and e_i^I is the ionization energy of ion species. The reference energy e_i^0 is taken to be standard heat of formation at 298 K [38].

3. Chemical kinetics

The chemical kinetics consists of the reaction mechanism and determines the net production rate of each species. For the chemical reactions of water vapor, we use the mechanism that were described in detail in Ref. [39]. Only a subset consisting of eight elementary reactions is used, corresponding to the first eight ones used by Yasui [24]. The first 19 reactions of Ref. [24] with additional species (HO₂, H₂O₂) were also tried but the resulting temperature was found to be a little lower than that from the 8 reaction scheme. The processes of nonequilibrium collisional ionization and recombination [40] are considered only for three monatomic species, noble gas, H, and O. The reason to choose H and O atoms is that they are quite ample in the water vapor dissociations, have lower ionization potentials, and can be treated using previous rate formulae. Ionizations of molecular species such as OH and H₂O are believed to be more complicated, thus are not accounted for. The net mass production rate $\dot{\omega}_k$ due to chemical reactions of the water vapor is determined by the law of mass action

$$\dot{\omega}_k = M_k \sum_{i=1}^{N_r} (\nu''_{ki} - \nu'_{ki}) q_i, \quad (9)$$

$$q_i = k_{fi} \prod_{k=1}^N \left(\frac{\rho_k}{M_k} \right)^{\nu'_{ki}} - k_{bi} \prod_{k=1}^N \left(\frac{\rho_k}{M_k} \right)^{\nu''_{ki}}, \quad (10)$$

where q_i is the net rate of progress of reaction i , and N_r the total number of reactions. The forward and backward reaction rate constants for the i th reaction k_{fi} and k_{bi} are given in Arrhenius form

$$k_{fi} = A_i^f T^{B_i^f} \exp(-C_i^f/T), \quad k_{bi} = A_i^b T^{B_i^b} \exp(-C_i^b/T). \quad (11)$$

Since the above rate constants as given in Ref. [39] are based on ideal gas, the modification for a van der Waals gas as suggested by Toegel *et al.* [28] is used. As they hinted, we can derive the equilibrium constant based on fugacity for a van der Waals gas [34]

$$K_{F_i} = \frac{K_{P_i}^{\text{ideal}}}{(1 - b\rho)^{\sum_{k=1}^N \nu_{ki}} \exp\left(-\frac{\sum_{k=1}^N \nu_{ki} b_k \rho_k}{1 - b\rho}\right)}. \quad (12)$$

where $\nu_{ki} = \nu''_{ki} - \nu'_{ki}$. Let the corrected forward rate frozen $k'_{f_i} = k_{f_i}$. We can obtain the corrected backward rate k'_{b_i} as

$$k'_{b_i} = \frac{k'_{f_i}}{K_{P_i}^{\text{ideal}}} = \frac{k_{b_i}}{(1 - b\rho)^{\sum_{k=1}^N \nu_{ki}} \exp\left(-\frac{\sum_{k=1}^N \nu_{ki} b_k \rho_k}{1 - b\rho}\right)}. \quad (13)$$

We will use k'_{f_i} and k'_{b_i} in Eq. (10). The Effects of the above modification suggested in Ref. [28] were found to suppress water vapor dissociation to some extent when compared with the raw rate constants k_{f_i} and k_{b_i} .

When involving the third-body reaction Eq. (10) becomes

$$q_i = \left[\sum_{k=1}^N Z_{k,i} \left(\frac{\rho_k}{M_k} \right) \right] \left[k'_{f_i} \prod_{k=1}^N \left(\frac{\rho_k}{M_k} \right)^{\nu'_{ki}} - k'_{b_i} \prod_{k=1}^N \left(\frac{\rho_k}{M_k} \right)^{\nu''_{ki}} \right], \quad (14)$$

where $Z_{k,i}$ is the third-body enhanced coefficient. Due to length limitation, the detailed formulas for net production rates and rate constants of collisional ionization, recombination, and three-body recombination are not given here. One can refer to Ref. [15, 40] for detail.

4. Mass and heat exchange at the bubble wall

The evaporation-condensation process and diffusion of the noble gas into the surrounding liquid are included. The net evaporation rate (mass per unit area and unit time) at the bubble wall is given as follows [20, 24]:

$$\dot{m}_e = \frac{\alpha_M}{\sqrt{2\pi R_v}} \left(\frac{P_{\text{sat}}(T_{l,\text{int}})}{\sqrt{T_{l,\text{int}}}} - \frac{\Gamma P_{v,\text{int}}}{\sqrt{T_{v,\text{int}}}} \right), \quad (15)$$

where α_M is the accommodation coefficient (evaluated using the formula in Ref. [24]) that shows which portion of water vapor molecules hitting the liquid surface is absorbed by this interface, R_v is the gas constant of water vapor, P_{sat} is the saturation vapor pressure at

liquid temperature $T_{l,\text{int}}$, $P_{v,\text{int}}$ is the partial pressure of water vapor, and Γ is the correction factor:

$$\Gamma = \exp(-\Omega^2) - \Omega\sqrt{\pi} \left(1 - \frac{2}{\sqrt{\pi}} \int_0^\Omega \exp(-x^2) dx \right), \quad (16)$$

$$\Omega = \frac{\dot{m}_e}{P_{v,\text{int}}} \sqrt{\frac{R_v T_{v,\text{int}}}{2}}. \quad (17)$$

In this study, the jump of temperature across the interface is assumed zero, thus $T_{l,\text{int}} = T_{v,\text{int}}$. Although Eq. (15) is valid only below a critical point (for water $T_{\text{cr}} \approx 647$ K), it is used throughout the whole acoustic cycle for simplicity. The rate of mass diffusion of the noble gas dissolved in the liquid at the wall is

$$\dot{m}_d = 4\pi R^2 D_l \left. \frac{\partial c}{\partial r} \right|_R, \quad (18)$$

where R is the bubble radius, D_l is the diffusion coefficient of the noble gas, and c is the mass concentration of the noble gas dissolved in the liquid.

The boundary conditions of species and energy at the bubble surface are derived by balancing the flux and source/sink of an interface control volume with infinitesimal thickness. In doing so, we assume that there are no uptakes of radical species or surface reactions. The resulting boundary condition for gas species is

$$-J_i|_R + \dot{m}_{\text{tot}} Y_i = \dot{m}_e f_i^e + \dot{m}_d f_i^d, \quad i = 1, \dots, N, \quad (19)$$

where

$$\dot{m}_{\text{tot}} = \dot{m}_e + \dot{m}_d, \quad f_i^e = \begin{cases} 1, & i = \text{water vapor} \\ 0, & i = \text{other species} \end{cases}, \quad f_i^d = \begin{cases} 1, & i = \text{noble gas} \\ 0, & i = \text{other species} \end{cases}. \quad (20)$$

The boundary condition of energy is

$$\left[\lambda \frac{\partial T}{\partial r} - \sum_{i=1}^N (J_i - \dot{m}_{\text{tot}} Y_i) h_i \right]_R + \dot{m}_e L - \dot{m}_d \Delta H = \lambda_l \left. \frac{\partial T_l}{\partial r} \right|_R, \quad (21)$$

where T_l and λ_l are the temperature and thermal conductivity of the liquid, respectively, L is the latent heat of evaporation of the liquid, and ΔH is the heat of solution of noble gas into the liquid [34, 41].

The gas and liquid velocities at the bubble surface and the velocity of the bubble wall differ due to mass transfer. The boundary condition for gas and liquid velocities are

$$u|_R = \dot{R} - \frac{\dot{m}_{\text{tot}}}{\rho}, \quad u_l|_R = \dot{R} - \frac{\dot{m}_{\text{tot}}}{\rho_l}. \quad (22)$$

The mass and heat transfer boundary conditions are nonlinear. All the boundary conditions for the gas dynamics have to be coupled with the following motion, temperature, and noble gas concentration equations in the surrounding liquid.

B. Motion, heat, and mass transport in the liquid

The liquid flow outside the spherical bubble is accounted for with different approximations for motion and heat (or mass) transport, respectively. On the one hand, the Euler equations for the liquid motion can be reduced to the ordinary differential equation for the bubble radius known as the RP equation. The RP equation is coupled with the NS equations through stress equilibrium condition at the bubble wall. On the other hand, we assume that the fluid is incompressible when accounting for heat and mass transfer in the liquid. The separate treatment reduces the complexity of solving a fully coupled hydrodynamic equations at sacrifice that shock waves in the liquid can not be simulated well.

Because the mass transfer at the bubble wall results in very small liquid velocity whose effect on the RP equation can be ignored, we let $u_l|_R = \dot{R}$. Thus we can use a form of the RP equation [42, 43] that includes first order terms in the Mach number $M = \dot{R}/C_{lb}$ and allows for variable speed of sound in the water [18, 44]:

$$(1 - M) R \ddot{R} + \frac{3}{2} \left(1 - \frac{1}{3} M\right) \dot{R}^2 = (1 + M) \left[H_b - \frac{1}{\rho_{l\infty}} P_s \left(t + \frac{R}{C_{l\infty}} \right) \right] + \frac{R}{C_{lb}} \dot{H}_b. \quad (23)$$

Here subscripts b and ∞ denote bubble wall and infinity, respectively, $P_s(t) = -P_a \sin(2\pi f t)$ is the pressure of the sound field with frequency f and amplitude P_a . For water, an equation of state of the modified Tait form

$$\frac{P + B}{P_\infty + B} = \left(\frac{\rho_l}{\rho_{l\infty}} \right)^n \quad (24)$$

is used with $B = 3049.13$ bar and $n = 7.15$. The enthalpy H_b and the speed of sound C_{lb} of the liquid at the bubble surface are given by

$$H_b = \int_{P_\infty}^{P_l} \frac{dP}{\rho_l} = \frac{n}{n-1} \left(\frac{P_{lb} + B}{\rho_{lb}} - \frac{P_\infty + B}{\rho_\infty} \right), \quad (25)$$

$$C_{lb}^2 = \frac{dP}{d\rho_l} \Big|_b = \frac{n(P_{lb} + B)}{\rho_{lb}}. \quad (26)$$

The pressure P_{lb} on the liquid side of the bubble surface is related to the pressure $P(R, t)$

on the gas side of the bubble surface by normal stress equilibrium condition

$$P(R, t) - \tau_{rr}|_{r=R} = P_{lb} + \frac{4\eta\dot{R}}{R} + \frac{2\sigma}{R} , \quad (27)$$

where η is the dynamic viscosity and σ is the surface tension. Their values depend on T_l , as formulated in the Appendix of Refs. [30, 41], respectively.

Both heat and mass transfer are taken into account although the former is found to be more important to the bubble dynamics. The equations for the water temperature and the mass concentration of dissolved noble gas take a similar form:

$$\frac{\partial T_l}{\partial t} + u_l \frac{\partial T_l}{\partial r} = \frac{\lambda_l}{\rho_l C_{P_l}} \frac{\partial}{\partial r} \left(r^2 \frac{\partial T_l}{\partial r} \right) , \quad (28)$$

$$\frac{\partial c}{\partial t} + u_l \frac{\partial c}{\partial r} = D_l \frac{\partial}{\partial r} \left(r^2 \frac{\partial c}{\partial r} \right) , \quad (29)$$

where C_{P_l} is the specific heat at constant pressure of the liquid. In Eqs. (28) and (29), the liquid velocity can be determined by the incompressible assumption

$$u_l = \frac{\dot{R}R^2}{r^2} . \quad (30)$$

The boundary condition for the water temperature are the continuity of heat flux Eq. (21) and $T_l|_{r=\infty} = T_\infty$, and the boundary condition for the mass concentration is

$$c|_{r=R} = \frac{c_0(T_\infty, P_0)}{P_0} P_{\text{no}}(R, t), \quad c|_{r=\infty} = c_\infty, \quad (31)$$

where c_0 is the saturated dissolved gas concentration at T_∞ and P_0 , and P_{no} is the partial pressure of the noble gas on the internal side of the bubble interface.

C. Numerical method

To exploit the advantage of a stationary Eulerian meshes, we use $x = r/R(t)$ to transform the NS equations (1) to a form in fixed domain $x \in [0, 1]$ as done in our earlier work [18]. The transport equations for water temperature T_l and mass concentration c in domain $r \in [R, \infty]$ are transformed into diffusion-type equations in domain $z \in [0, 1]$ through two consecutive coordinate transformations [45, 46] with the aid of Eq. (30). The details were given in Refs. [18, 47].

We apply the second-order upwind total-variational-diminishing (TVD) scheme [48] to the inviscid flux terms and the central difference to the diffusive terms of the NS equations.

The temporal discretization differs from Ref. [18] in that we now use an Adams-Bashforth explicit scheme for the convective and spherical coordinate terms, and Crank-Nicolson implicit scheme for diffusive and chemical source terms. The implicit treatment is to overcome the stiffness problem due to diffusive transport and chemical source terms. The trapezoidal rule and central difference are used for the water temperature and concentration equations. A predictor-corrector method is used for the RP equation. We use 400 grid points for the NS equations and 100 points for the water temperature and gas concentration equations.

III. OPTICAL POWER RADIATED BY THE BUBBLE

We compute SBSL based on the weakly ionized gas model of Hilgenfeldt *et al.* [8], which was most thoroughly studied and remarkably successful [10]. In more general cases with nonuniform bubble interior, the bubble has an optically thin radiating/absorbing outer shell, and may have a blackbody inner core when the opacity is large enough [11, 12]. We previously applied this generic version to a pure argon bubble [14, 15]. In this paper, we apply the formulas of photon absorption coefficients [8, 49] to the gas mixture in the bubble. The overall photon absorption coefficient $\kappa_\lambda^{\text{tot}}$ is the sum of contributions from all species

$$\kappa_\lambda^{\text{tot}} = \sum_{i=1}^N \kappa_{\lambda,i} = \sum_{i=1}^N \left(\kappa_{\lambda,i}^{\text{ff}+} + \kappa_{\lambda,i}^{\text{ff}0} + \kappa_{\lambda,i}^{\text{bf}} \right), \quad (32)$$

where $\kappa_{\lambda,i}^{\text{ff}+}$ is the absorption due to the free-free interaction of electron and ions, $\kappa_{\lambda,i}^{\text{ff}0}$ is the absorption due to free-free interactions of electrons and neutral atoms, and $\kappa_{\lambda,i}^{\text{bf}}$ is the absorption by bound-free ionization of already excited atoms. The ionization potentials used can be found in Ref. [50]. The bound-bound absorption is not accounted for and the modification to electron-neutral-atom bremsstrahlung [9, 51] is not adopted for the time being.

The finite opacity model given in Refs. [14, 15] (without the Θ correction) is used to compute the total spectral radiance (power emitted per wavelength interval) of the bubble content at wavelength λ

$$\begin{aligned} P_\lambda^{\text{Pl}}(t) = & \int_{R_c}^R 16\pi \kappa_\lambda^{\text{tot}}(r, t) R_\lambda^{\text{Pl}}(r, t) \exp \left(- \int_r^R \kappa_\lambda^{\text{tot}}(r', t) dr' \right) r^2 dr \\ & + 4\pi R_c^2 R_\lambda^{\text{Pl}}(R_c, t) \exp \left(- \int_{R_c}^R \kappa_\lambda^{\text{tot}}(r, t) dr \right), \end{aligned} \quad (33)$$

where

$$R_\lambda^{\text{Pl}}[T(r, t)] = \frac{2\pi hc^2}{\lambda^5} \frac{1}{\exp(hc/\lambda k_B T) - 1} \quad (34)$$

is the spectral emissive power (energy per unit time, wavelength interval, and projected surface area) with the Planck and Boltzmann constants h and k_B , and the light speed in vacuum c . The time-dependent radius of the blackbody core R_c can be defined by the expression [12]

$$\int_{R_c}^R \bar{\kappa}^{\text{tot}}(r, t) dr = 1, \quad (35)$$

where $\bar{\kappa}^{\text{tot}}$ is the wavelength-averaged absorption coefficient between 200 and 800 nm. Equation (35) implies that if radiation from a spherical surface at depth R_c is damped to some extent (the optical depth being 1), then radiation from further interior is completely opaque to an outside observer. The spherical surface R_c serves as the surface of a blackbody in place of radiations from the interior. The determination of R_c starts from the outermost. If $\bar{\kappa}^{\text{tot}}$ is sufficiently large, there will be a finite-size blackbody core $0 < R_c \leq R$ such that Eq. (35) is satisfied; if $\bar{\kappa}^{\text{tot}}$ is small, the left hand side of Eq. (35) will be less than 1 even if $R_c=0$, implying that the bubble is optically thin. The calculated photon absorption coefficients indicate that the bubble is always optically thin, $R_c \equiv 0$. However, in order to see how a finite-size blackbody model behaves, we intentionally amplify $\bar{\kappa}^{\text{tot}}$ by a free parameter E_c so that

$$\int_{R_c}^R E_c \cdot \bar{\kappa}^{\text{tot}}(r, t) dr = 1 \quad (36)$$

will give a nonzero R_c during the collapse stage. It is evident that larger E_c makes R_c closer to R . With $R_c(t)$ at hand, we can calculate the light emission by Eq. (33) together with original $\kappa_\lambda^{\text{tot}}$, whose small quantity makes the second term in Eq. (33) dominant. For convenience of discussion we denote $R_c \equiv 0$ as the optically thin model and $R_c > 0$ as the finite-size blackbody model. It is remarked that the finite-size blackbody model is physical if $E_c = 1$, and is *ad hoc* if $E_c > 1$. For fitting purpose, E_c is different from case to case but remains fixed during an acoustic cycle.

It is meaningful to look at the light pulses and spectra. The integration of the spectral radiance over a suitable wavelength intervals ($\lambda_{\text{UV}} = 200 \text{ nm} \sim \lambda_r = 800 \text{ nm}$) gives the total power emitted into the measurable part of the spectrum, and integration over one acoustic

period T_s gives the light spectrum that can be compared with the experimental results

$$P^{\text{Pl}}(t) = \int_{\lambda_{\text{UV}}}^{\lambda_r} P_{\lambda}^{\text{Pl}}(t) d\lambda, \quad S_{\lambda}^{\text{Pl}} = \frac{1}{T_s} \int_0^{T_s} P_{\lambda}^{\text{Pl}}(t) dt \quad (37)$$

IV. NUMERICAL RESULTS

It is well known that the ambient bubble radius R_0 depends on experimentally controllable parameters such as the driving pressure amplitude P_a , the water temperature T_{∞} , and the gas concentration dissolved in the water c_{∞} . A problem with past SL spectrum measurements was they seldom gave the key parameters P_a and R_0 at the same time. This left freedom for theoretical studies to fit experimental data using different P_a and R_0 . The present study tries to use the same parameters as those in previous literatures. For comparison with other calculations, the parameters used here are $P_a = 1.2$ bar, $T_{\infty} = 298$ K (Storey [26]) and $P_a = 1.35$ atm, $T_{\infty} = 300$ K (Xu [31]) for identical equilibrium radius $R_0 = 4.5 \mu\text{m}$ and driving frequency $f = 26.5$ kHz, and $P_a = 1.4$ bar for $R_0 = 6.0 \mu\text{m}$, $f = 20.6$ kHz, $T_{\infty} = 293.15$ K (Moss [12]). The dissolved gas concentration is $c_{\infty}/c_0 = P_{\text{no}\infty}/P_0 = 0.395\%$ (3 Torr partial pressure) for all above cases. For comparison with the experiment [16], $R_0 = 4.5 \mu\text{m}$ (He), $5.5 \mu\text{m}$ (Xe), $f = 42$ kHz, $T_{\infty} = 296.15$ K, $P_{\text{no}\infty} = 150$ Torr (He) and 3 Torr (Xe), while P_a is adjustable. Other parameters are $P_{\infty} = 101325$ Pa, $\rho_{l\infty} = 996.6 \text{ kg m}^{-3}$, $k_l = 0.609 \text{ W m}^{-1} \text{ K}^{-1}$, $C_{Pl} = 4179 \text{ J kg}^{-1} \text{ K}^{-1}$, and $D_l = 2 \times 10^{-9} \text{ m}^2/\text{s}$. The van der Waals excluded volumes are given in Table I. Initial number densities of ions and electrons are estimated using the Saha equation [49]. The initial bubble content contains 2% molar fraction water vapor. This number seems arbitrary, but our results are based on the second acoustic cycle when initial disturbances are presumed to be decayed.

TABLE I: van der Waals excluded volumes.

Species	He & ions	Ar & ions	Xe & ions	H ₂ O	OH	H	H ⁺	O	O ⁺	H ₂	O ₂	e ⁻
\tilde{b}_i (cm ³ /mol)	23.7	32.2	51.0	30.5	15.25	4.98	36.8	2.77	27.7	26.6	31.8	0.0

A. Effects of chemical reactions

Figure 1 shows one forcing period of the radius of an argon bubble corresponding to case I (pure noble gas in the bubble), case II (with water vapor but no chemical reactions), and case III (with water vapor and chemical reactions) as labeled in Ref. [26]. One can see that the difference between II and III is almost indiscernible, but that between I and the latter two is large. The existence of water vapor increases the maximum radius and delays the collapse. In spite of little difference between II and III in the R - t curve, large difference occurs for thermodynamic variables at collapse. Table II shows comparison of some quantities. The maximum radius of the present calculation is smaller than that of Story [26]. This is mainly because the acoustic forcing terms in Eq. (23) is separate from H_b rather than absorbed in P_∞ as treated in Refs. [26, 35] that magnified P_a by a factor of $n/(n-1)$ [see Eq. (25)]. Since there are much differences between the present model and Storey's, quantitative discrepancies are expectable for the extreme values. Both models predicted temperature reduction from case I to III. However, the present result show that temperature is slightly reduced from I to II, but heavily from II to III. The slight reduction is due to the compensating effects of increased compression ratio (R_{\max}/R_{\min}) and reduced ratio of specific heats [26]. The larger reduction from 17 000 K (case II) to 8900 K (case III) indicates the significant effect of chemical reactions in reducing the temperature.

TABLE II: Comparison of extreme values for an argon bubble $R_0 = 4.5 \mu\text{m}$, $P_a = 1.2$ bar. The amount of water vapor in II is in mole fraction and evaluated at the moment of R_{\min} .

case	$R_{\max}/R_{\min}(\mu\text{m})$		T_{\max} (K)		total vapor (%)	
	present	Ref. [26]	present	[26]	present	[26]
I	25.4/0.88	28.0/0.80	17900	20900		
II	28.7/0.76	31.3/0.70	17000	9700	7.7	14 ^a
III	28.9/0.70	31.7/0.65	8900	7000		

^aReference [26] did not specify the exact moment for this value.

The effects of chemical reactions on thermodynamic variables are best reflected in the distributions of temperature and chemical yields inside the bubble. Figure 2 shows snapshots of the spatial profiles of temperature around the moment of minimum bubble radius. It can

be seen that temperatures are considerably reduced in the reacting case III. Figure 3 shows the numbers of molecules of different species and temperature at the bubble center as a function of time. Note that in the first acoustic cycle the water vapor begins to dissociate appreciably at $t = -2 \sim -1$ ns, while in the beginning of the second cycle there are already some amounts of H_2 and O_2 gases accumulated. The chemical reactions occur in a time scale of several nanoseconds, producing considerable amounts of H, O, OH radicals and H_2 and O_2 gases. It is remarked that the prediction of chemical products is very difficult as the reaction mechanisms and phase change processes are largely unknown under extreme conditions in a SL bubble.

Next we compare a $R_0 = 6.0 \mu\text{m}$ Ar bubble driven at $P_a = 1.4$ bar, which was labeled as A1 in Ref. [12]. The present temperatures at the bubble center are respectively 109 600 K, 34 700 K, and 16 200 K for cases I–III in Fig. 1, suggesting that both the reduced ratio of specific heats due to the presence of water vapor and the chemical reactions contribute significantly to the reduction of temperatures. The amount of trapped water vapor at the moment of R_{\min} for case II occupies 23% molar fraction, smaller than 33 % [26]. Figure 4 shows several snapshots of the spatial profiles of thermodynamic variables. A main feature is that only compression waves occur. As seen from the velocity profile, a compression wave moves outward at t_4 and t_5 , reflects from the bubble wall and moves inward at t_6 . This result is different from that of Moss *et al.* [12], where shock waves were reported. A possible reason is that the formation of a shock is sensitive to differences in equations of state, accommodation coefficients, chemical reactions, and treatments of the liquid motion, and so on. Another feature in Fig. 4 is that the temperature in the inner zone is reduced more severely than in the outer zone at t_1, t_2, t_7 , and t_8 when the compression wave is not strong. This is because considerable water vapor is trapped in the inner zone of an Ar bubble as a result of thermal diffusion [31, 35] (which states that a heavier species tends to diffuse toward the cooler region) and dissociates there, thus peak temperature is not at the center, but at some place close to the bubble interface. For a lighter-than-water-vapor He bubble, less water vapor is congregated in the central zone, and temperature peak will be located at the bubble center as [will be shown in Fig. 6 (b)]. Figure 5 shows one snapshot of the number density distributions and the degrees of ionization. It can be seen that the amounts of products due to chemical reactions are considerable, while the degrees of ionization are quite small (the maximum being 2.8% for O^+), contrary to significant ionizations when water

vapor was not taken into account [15]. The degrees of ionization of H and O far exceed that of Ar although Ar atom is more ample in quantity.

The numerical results in this subsection demonstrates that the trapped water vapor and the ensuing endothermic chemical reactions significantly reduce the temperature, resulting in very low degrees of ionization. The chemical reactions can produce considerable amounts of atomic and molecular species, some of which, such as H and O atoms, are easier to ionize than a noble gas atom such as He or Ar. As the evaporation is a robust process in the bubble oscillation, chemical radicals will have significant influence on SBSL mechanism as will be shown in Sec. IV C.

B. Effects of noble gas types

Previous numerical studies pointed that shock formation depends sensitively on, among other factors [18], the amount of water vapor [12, 31] and its distribution [26]. Xu *et al.* [31] showed that shock waves develop in a bubble filled with 70% Xe and 30% (mole fractions) water vapor, but no shocks occur for similarly filled Ar or He bubbles. With evaporation-condensation process and chemical reactions taken into account, we are able to investigate effects of noble gases on the thermodynamic processes more realistically. We calculated Xe, Ar and He bubbles using the same R_0 , P_a , f , and T_∞ as those in Ref. [31].

Figures 6(a) and 6(b) show snapshots of the spatial profiles of thermodynamic variables around the moment of minimum bubble radius for Xe and He bubbles. Snapshots of the Ar bubble are similar to those in Fig. 4, thus are not shown here. In the Xe bubble [Fig. 6(a)], it is seen that an inward-going compression wave at t_2 evolves into a strong outward-going shock at t_3 . The first focusing of the shock happened between t_2 and t_3 leads to extreme high temperatures ($> 10^6$ K), but the duration is very short (< 1 ps) and the region is confined to the center ($r < 0.005 \mu\text{m}$). However, Fig. 6(b) shows that only weak compression waves occur in the He bubble. These results are in qualitative agreement with those of Xu *et al.* [31]. Note that the temperature peaks are often at the center in He bubble except when a wavy disturbance reflects from the bubble wall at t_4 . This feature mainly results from the thermal diffusion between the light He gas and the heavy water vapor as mentioned in previous subsection.

Figure 7(a) and 7(b) show one snapshot of the number density and the compositional

distributions at the moment of minimum bubble radius for Xe and He bubbles. In both bubbles there are significant numbers of chemical products, especially H, O, OH, and H₂. However, the right figure in Fig. 7(a) indicates that atomic species in Xe bubble are significantly ionized only in the central zone ($r < 0.07R$), while the right figure in Fig. 7(b) shows that the degrees of ionization in He bubble are small, especially that for He gas. The situation for Ar bubble is found to be in between [Fig. 5(b)]. This suggests that chemical products of the water vapor may play an increasingly important role in SBSL from Xe, Ar, to He bubbles.

C. Calculated light spectra and pulses

We shall compute the emitted lights by using the optically thin model and the *ad hoc* finite-size blackbody model. We fit our calculations to Fig. 2 of a recalibrated experiment [16] under the same parameters as given in the beginning of this section. The former model has only P_a while the latter has P_a and E_c in Eq. (36) as fitting parameters.

Figure 8 shows comparison of the spectral radiances. It is seen that the optically thin model does not match well with the experimental spectrum of Xe bubble, but the finite-size blackbody model matches well. The fitting $P_a = 1.55$ atm of the optically thin model seems to be out of the stable SBSL range (1.2 – 1.5 atm), while the fitting $P_a = 1.28$ atm of the *ad hoc* finite-size blackbody is within the range, of course with the help of a large value $E_c = 1.8 \times 10^4$. (Fitting using $P_a = 1.49$ atm and a smaller value, $E_c = 60$ can also give similar spectrum but the resulting FWHM is only 40 ps, much shorter than experimental 200 ps.) However, it can be seen that either models are unable to fit the spectrum of He bubble. The finite-size blackbody is much better than the optically thin model as the latter deviates severely from the experiment. The maximum temperatures at $P_a = 1.28$ atm for Xe bubble and at $P_a = 1.45$ atm for He bubble are 8600 and 16 700 K, respectively, which are comparable to the blackbody fitting temperatures 8000 (Xe) and 20 400 K (He) used in Ref. [16].

Figure 9 compares the time variations of the normalized power for the “measurable,” “UV” (300–400 nm), and “red” (590–650 nm) wavelength intervals [4]. Both models show good wave-length independence of light pulse, a key ingredient of SBSL thought by several researchers [4, 8]. One curves “A,” the optically thin model gives FWHM of 26 ps for Xe

bubble, and 13 ps for He bubble, which are much shorter than the experimental flash widths of 200 ps (Xe) and 100 ps (He) [16]. On curves “B,” the finite-size blackbody model predicts FWHM of 185 ps for Xe bubble, and 18 ps for He bubble, better than the optically thin model. Figure 10 shows the variations of the blackbody core and bubble radius with time. One can see that the blackbody core appears abruptly, attains maximum around the moment of minimum bubble radius, and disappears suddenly. The short life of the blackbody core explains why this blackbody model also shows wave-length independence of the light pulse similar to the optically thin model: The quick rise and fall of R_c in accordance with the variation of the photon absorption coefficients cut down the long fall time for red light [8].

Figure 11 shows the visible light powers contributed from the total and partial species as computed by the optically thin model. In Fig. 11(a) we see that the power from xenon is dominant, while that from the water vapor and its chemical products contributes a little. But in Fig. 11(b), the power from helium is small, while the water vapor and its chemical products contribute dominantly with H and O radicals being the primary ones. Although the absolute values of the light powers from the optically thin model are quite small, the relative contributions to the total power verify previous postulation that light emission from radicals generated from water vapor dissociation may dominate SBSL in the He bubble [8].

The failure of the optically thin model to match with the experiment and the improvement by adding an *ad hoc* finite-size blackbody core to it raise contradiction. The major reason for the failure of the optically thin model is the significant reduction of temperature due to the existence of water vapor and endothermic chemical reactions. We remark that the present *ad hoc* blackbody is not the unique way for better fitting, but is shown better than other *ad hoc* ways such as multiplying the photon absorption coefficient by an arbitrary factor. We did not exclude the possibility that the optically thin model could fit well to the experimental data should higher temperature or increased opacity be obtained in whatever a natural way. As a numerical study, we have made tests of model sensitivity to parameters. The evaporation-condensation process and chemical reaction rates are important for the modeled temperature. We used the accommodation coefficient $\alpha_M = 0.4$ [26] as well as the formula [24], and found that the former led to higher temperature so that we could use $P_a = 1.7$ atm to obtain the same spectrum of He bubble as the one obtained by using $P_a = 2.0$ atm in Fig. 8. However, the results were still unable to fit to the data. As to the chemical reaction rates, we compared two different reaction rate sets [24, 39]. There was slight difference in

quantity and what we presented here was the one corresponding to higher temperature [39]. We have already adopted the modified chemical equilibrium constant (12) for a van der Waals gas. This modification was claimed to let the optically thin model give sufficient light emission [28], but we found while it raised temperature to some extent, it could not result in enough light emission. Therefore, it will be better to pursue other ways to reconcile the conflict. One conjecture was if there existed a mechanism that would greatly increase the photon absorption coefficient of the highly compressed bubble content [3, 16], such as the lowering of ionization potentials [10]. it is also wished to have better theories to compute the photon absorption coefficients of a very dense gas mixture, and to take into account other light emission processes due to the existence of chemical products. Meanwhile further efforts are necessary to reduce modelling uncertainties such as the chemical reaction rates under high-pressure and high-temperature conditions, and the description of the surrounding liquid motion. The RP equation approach in this and other studies [26] should be more critically compared with the full hydrodynamic equation approach [12, 13].

V. CONCLUSIONS

A refined hydrochemical model is presented to simulate the complex processes inside a sonoluminescing bubble. The numerical simulations of Xe, Ar, and He bubbles indicate that the trapped water vapor and its endothermic reactions reduce the temperature significantly. In the stable SBSL range, at most compression waves can appear in He or Ar bubbles, while shock waves can occur in Xe bubbles only for higher driving amplitudes. The lower temperature in the bubble rarely leads to appreciable ionization except for Xe bubble at the center during the shock wave focusing. The chemical radicals generated from water vapor dissociations become increasingly important in the light emission from Xe, Ar, to He bubbles. Particularly, H and O radicals are shown to be the primary light-emitting matters in He bubbles.

The key finding of this study is that the optically thin thermal emission model was unable to match with experimental data mainly due to the reduced temperatures in the bubble. The introduction of a finite-size blackbody core made the calculated light spectra and pulse widths match better with experimental ones. The present expertise to define an optically thick region is *ad hoc* and only serves to illustrate one possible improving direction. Im-

provements by physical considerations such as the lowering of ionization potentials and the refinement of the photon absorption processes under the extreme conditions of sonoluminescence, and by reduction of modeling uncertainties, are worthy of further investigation.

Acknowledgments

The author thanks M.-C. Chu and Yu An for meaningful discussions. This work is supported by National Natural Science Foundation of China (Grant Nos. G10172089, G10476032) and State Key Program of Basic Research (Grant No. G1999032801).

-
- [1] D. Gaitan, L. Crum, C. Church, and R. Roy, *J. Acoust. Soc. Am.* **91**, 3166 (1992).
 - [2] B. Barber, R. Hiller, R. Löfstedt, S. Putterman, and K. Weninger, *Phys. Rep.* **281**, 65 (1997).
 - [3] M. Brenner, S. Hilgenfeldt, and D. Lohse, *Rev. Mod. Phys.*, **74**, 425 (2002).
 - [4] B. Gompf, R. Günther, G. Nick, R. Pecha, and W. Eisenmenger, *Phys. Rev. Lett.* **79**, 1405 (1997).
 - [5] R. Hiller, S. Putterman, and K. Weninger, *Phys. Rev. Lett.* **80**, 1090 (1998).
 - [6] M. Moran and D. Sweider, *Phys. Rev. Lett.* **80**, 4987 (1998).
 - [7] S. Hilgenfeldt, S. Grossmann, and D. Lohse, *Nature (London)* **398**, 402 (1999).
 - [8] S. Hilgenfeldt, S. Grossmann, and D. Lohse, *Phys. Fluids* **11**, 1318 (1999). We note that the term “vacuum permeability” denoted as ϵ_0 in this reference as well as in Ref. [15] should be the “vacuum permittivity” consistent with [49].
 - [9] D. Hammer and L. Frommhold, *Phys. Rev. Lett.* **85**, 1326 (2000).
 - [10] D. Hammer and L. Frommhold, *J. Mod. Opt.* **48**, 239 (2001).
 - [11] W. Moss, D. Clarke, and D. Young, *Science* **276**, 1398 (1997).
 - [12] W. Moss, D. Young, J. Harte, J. Levatin, B. Rozsnyai, G. Zimmerman, and I. Zimmerman, *Phys. Rev. E* **59**, 2986 (1999).
 - [13] P. Burnnet, D. Chambers, D. Heading, A. Machacek, M. Schnittker, W. Moss, P. Young, S. Rose, R. Lee, and J. Wark, *J. Phys. B* **34**, L511 (2001).
 - [14] C. Y. Ho, L. Yuan, M.-C. Chu, P. T. Leung, and W. Wei, *Europhys. Lett.* **56**, 891 (2001).
 - [15] C. Y. Ho, L. Yuan, M.-C. Chu, P. T. Leung, and W. Wei, *Phys. Rev. E* **65**, 041201 (2002).

- [16] G. Vazquez, C. Camara, S. Putterman, and K. Weninger, Opt. Lett. **26**, 575 (2001).
- [17] V. Vuong and A. Szeri, Phys. Fluids **8**, 2354 (1996).
- [18] L. Yuan, H. Y. Cheng, M.-C. Chu, and P. T. Leung, Phys. Rev. E **57**, 4265 (1998).
- [19] H. Y. Cheng, M.-C. Chu, P.T. Leung, and L. Yuan, Phys. Rev. E **58**, R2705 (1998).
- [20] S. Fujikawa and A. Akamatsu, J. Fluid Mech. **97**, 481 (1980).
- [21] V. Kamath, A. Prosperetti, and F. Egolfopoulos, J. Acoust. Soc. Am. **94**, 248 (1993).
- [22] S. Sochard, A. Wilhelm, and H. Delmas, Ultrason. Sonochem. **4**, 77 (1997).
- [23] C. Gong and D. Hart, J. Acoust. Soc. Am. **104**, 2675 (1998).
- [24] K. Yasui, Phys. Rev. E **56**, 6750 (1997).
- [25] K. Suslick, Y. Didenko, M.F. Fang, T. Hyeon, K. Kolbeck, W. McNamara, M. Mdleleni, and M. Wong, Philos. Trans. R. Soc. London, Ser. A **357**, 335 (1999).
- [26] B. Storey and A. Szeri, Proc. Roy. Soc. London, Ser. A **456**, 1685 (2000).
- [27] R. Toegel, B. Gompf, R. Pecha, and D. Lohse, Phys. Rev. Lett. **85**, 3165 (2000).
- [28] R. Toegel, S. Hilgenfeldt, and D. Lohse, Phys. Rev. Lett. **88**, 034301 (2002).
- [29] C. C. Xie, Y. An, and C. F. Ying, Acta Phys. Sin. **52**, 102 (2003).
- [30] I. Akhatov, O. Lindau, A. Topolnikov, R. Mettin, N. Vakhitova, and W. Lauterborn, Phys. Fluids **13**, 2805 (2001).
- [31] N. Xu, R. Apfel, A. Khong, X. W. Hu, and L. Wang, Phys. Rev. E. **68**, 016309 (2003).
- [32] T. Poinso and D. Veynante, *Theoretical and Numerical Combustion*, (R.T. Edwards, Flouertown, PA, 2001).
- [33] J. Hirschfelder, C. Curtiss, and R. Bird, *Molecular theory of gases and liquids* (Wiley, New York, 1954).
- [34] R. Reid, J. Prausnitz, and T. Sherwood, *The properties of gases and liquids*, 3rd ed. (McGraw-Hill, New York, 1977).
- [35] B. Storey and A. Szeri, J. Fluid Mech. **396**, 203 (1999).
- [36] R. Gupta, J. Yos, and R. Thompson, "A review of reaction rates and thermodynamic and transport properties for the 11-species air model for chemical and thermal nonequilibrium calculations to 30 000 K", NASA TM 101528, 1989 (unpublished).
- [37] C. C. Wu and P. Roberts, Phys. Rev. Lett. **70**, 3424 (1993).
- [38] Smith G *et al.*, GRI-Mech 3.0, 1999, http://www.me.berkeley.edu/gri_mech/
- [39] J. Evans and C. Schexnayder, AIAA J. **18**, 188 (1980).

- [40] N. Xu, L. Wang, and X. W. Hu, Phys. Rev. Lett. **83**, 2441 (1999).
- [41] K. Yasui, J. Phys. Soc. Jpn. **65**, 2830 (1996).
- [42] J. Keller and M. Miksis, J. Acoust. Soc. Am. **68**, 628 (1980).
- [43] A. Prosperetti and A. Lezzi, J. Fluid Mech. **168**, 457 (1986).
- [44] V. Kamath and A. Prosperetti, J. Acoust. Soc. Am. **85**, 1538 (1987).
- [45] M. Plesset and S. Zwick, J. Appl. Phys. **23**, 95 (1952).
- [46] C. Grosh and S. Orszag, J. Comput. Phys. **25**, 273 (1977).
- [47] S. Hilgenfeldt, D. Lohse, and M. Brenner, Phys. Fluids **8**, 2808 (1996).
- [48] H. C. Yee, “A class of high-resolution explicit and implicit shock-capturing methods”, NASA TM 101088, 1989 (unpublished).
- [49] Y. Zeldovich and Y. Raizer, *Physics of Shock Waves and High-temperature Hydrodynamic Phenomena*, edited by W. D. Hayes and R. F. Probstein (Academic Press, New York, 1966), Vol.1.
- [50] S. C. Brown, *Basic data of plasma physics* (MIT Press, Cambridge, 1966).
- [51] L. Frommhold, Phys. Rev. E **58**, 1899 (1998).

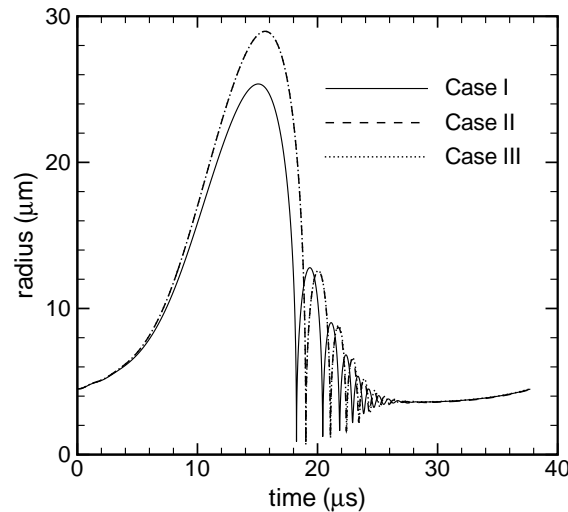


FIG. 1: Radius of an argon bubble vs time over one acoustic period for the same parameters as used in Ref. [26]: $R_0 = 4.5 \mu\text{m}$, $P_a = 1.2 \text{ bar}$, $f = 26.5 \text{ kHz}$, $T_\infty = 298 \text{ K}$. Case I: without phase change and chemistry; case II: with phase change but without chemistry; case III: with phase change and chemistry.

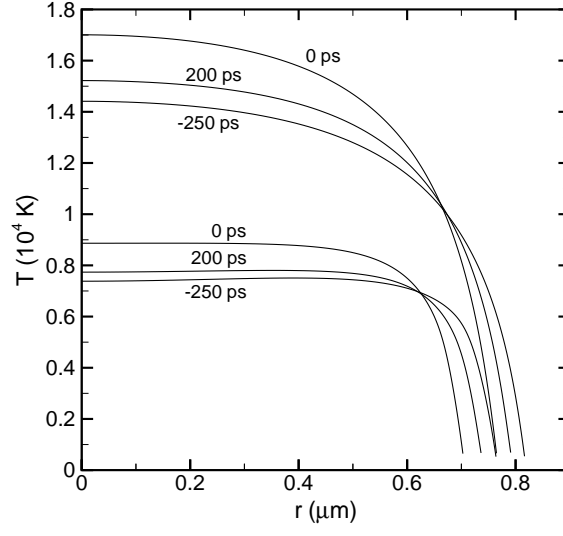


FIG. 2: Snapshots of the temperature distributions for Ar bubble at $P_a = 1.2$ bar, $R_0 = 4.5 \mu\text{m}$. The upper three lines are for nonreacting case II, and the lower three lines are for reacting case III. $t = 0$ ps corresponds to the time of minimum radius ($t_{\min} = 19.015945 \mu\text{s}$).

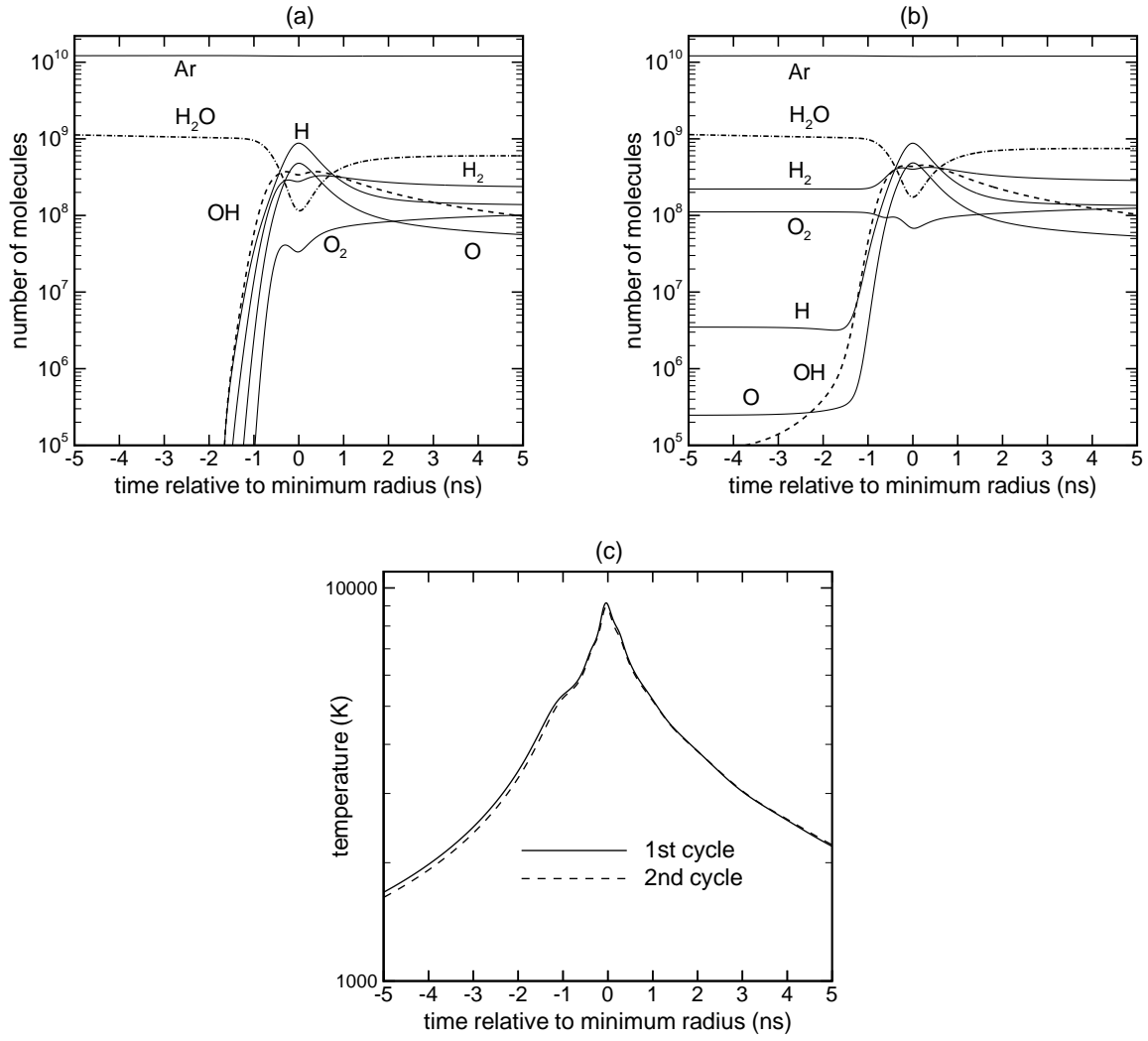


FIG. 3: The numbers of molecules of species and the temperature of the center around the moment of minimum bubble radius as a function of time for Ar bubble at $P_a = 1.2$ bar, $R_0 = 4.5 \mu\text{m}$. (a) First acoustic cycle, (b) second acoustic cycle, (c) temperature at the bubble center.

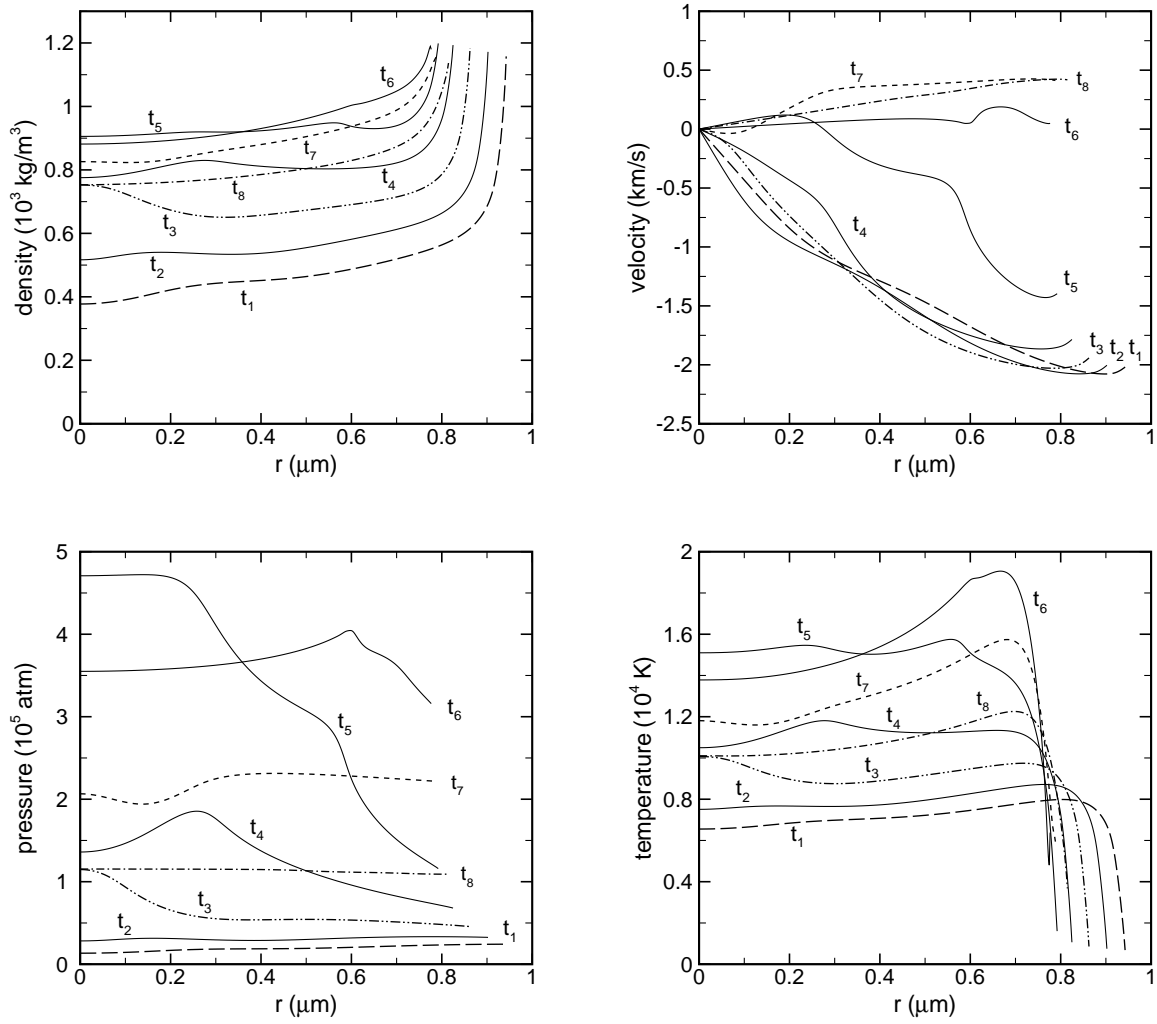


FIG. 4: Snapshots of the spatial profiles of density, velocity, pressure, and temperature for $P_a = 1.4$ bar, $R_0 = 6 \mu\text{m}$. Time sequences are $t_1 = -100$ ps, $t_2 = -80$ ps, $t_3 = -60$ ps, $t_4 = -40$ ps, $t_5 = -20$ ps, $t_6 = 0$ ps, $t_7 = 40$ ps, $t_8 = 100$ ps, where $t_6 = 0$ denotes the time of minimum radius ($t_{\min} = 28.970309 \mu\text{s}$).

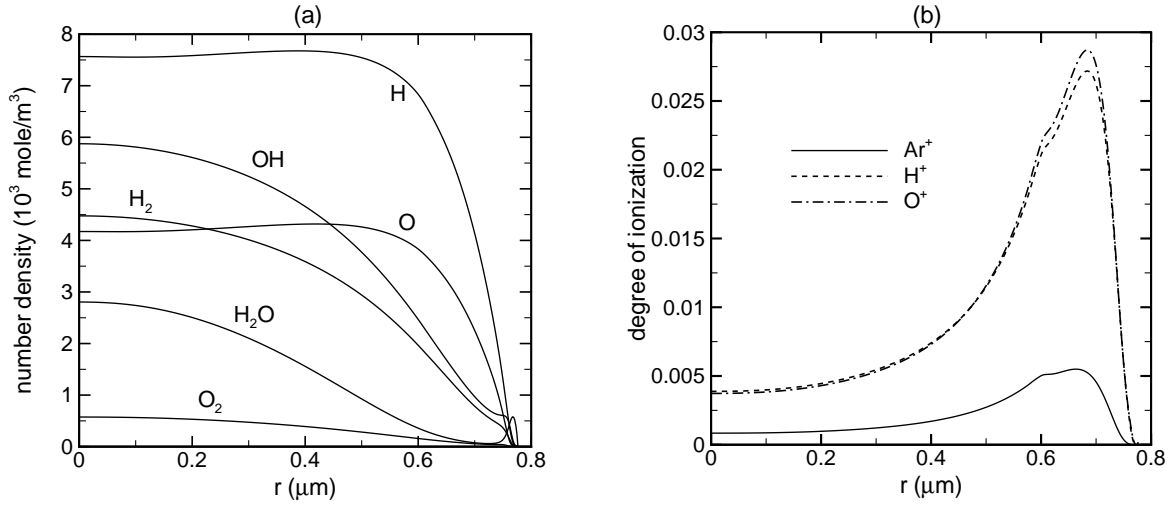
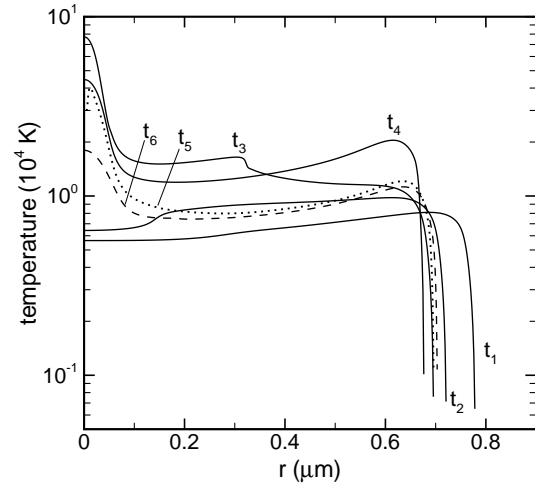
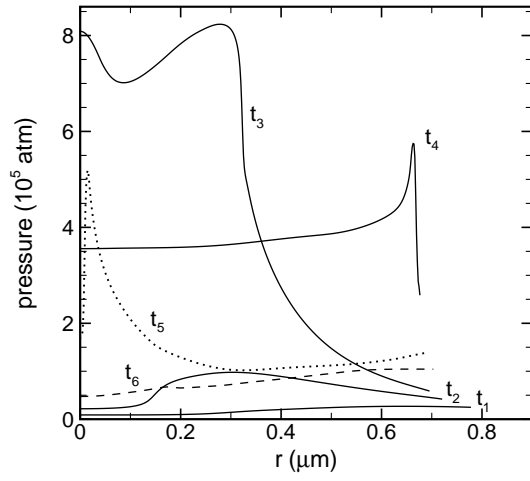
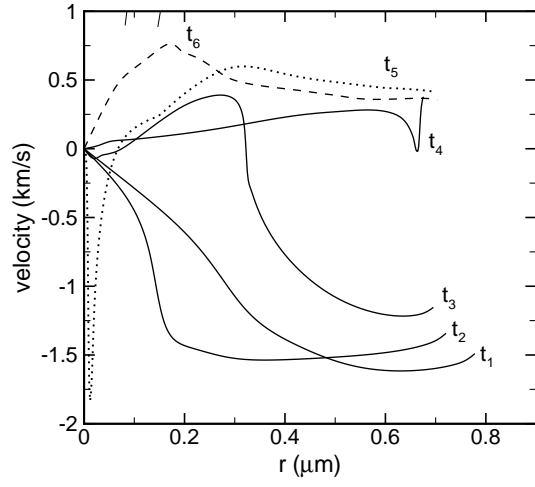
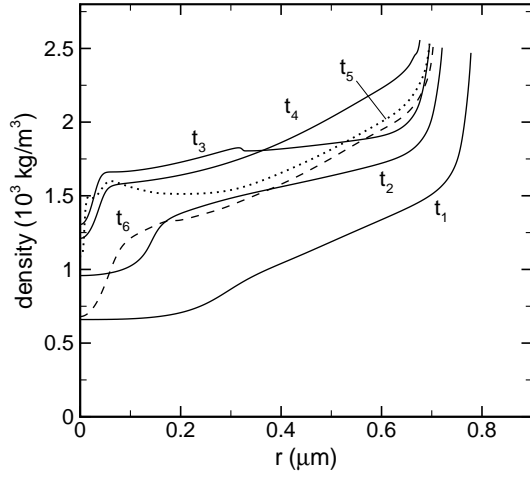


FIG. 5: The spatial profiles of number densities for molecular species (a) and degrees of ionization for ionic species (b) at the time of minimum bubble radius $t = 0$ ($t_{\min} = 28.970309 \mu\text{s}$) for $P_a = 1.4 \text{ bar}$, $R_0 = 6 \mu\text{m}$. The degree of ionization is computed using the Saha equation.

(a)



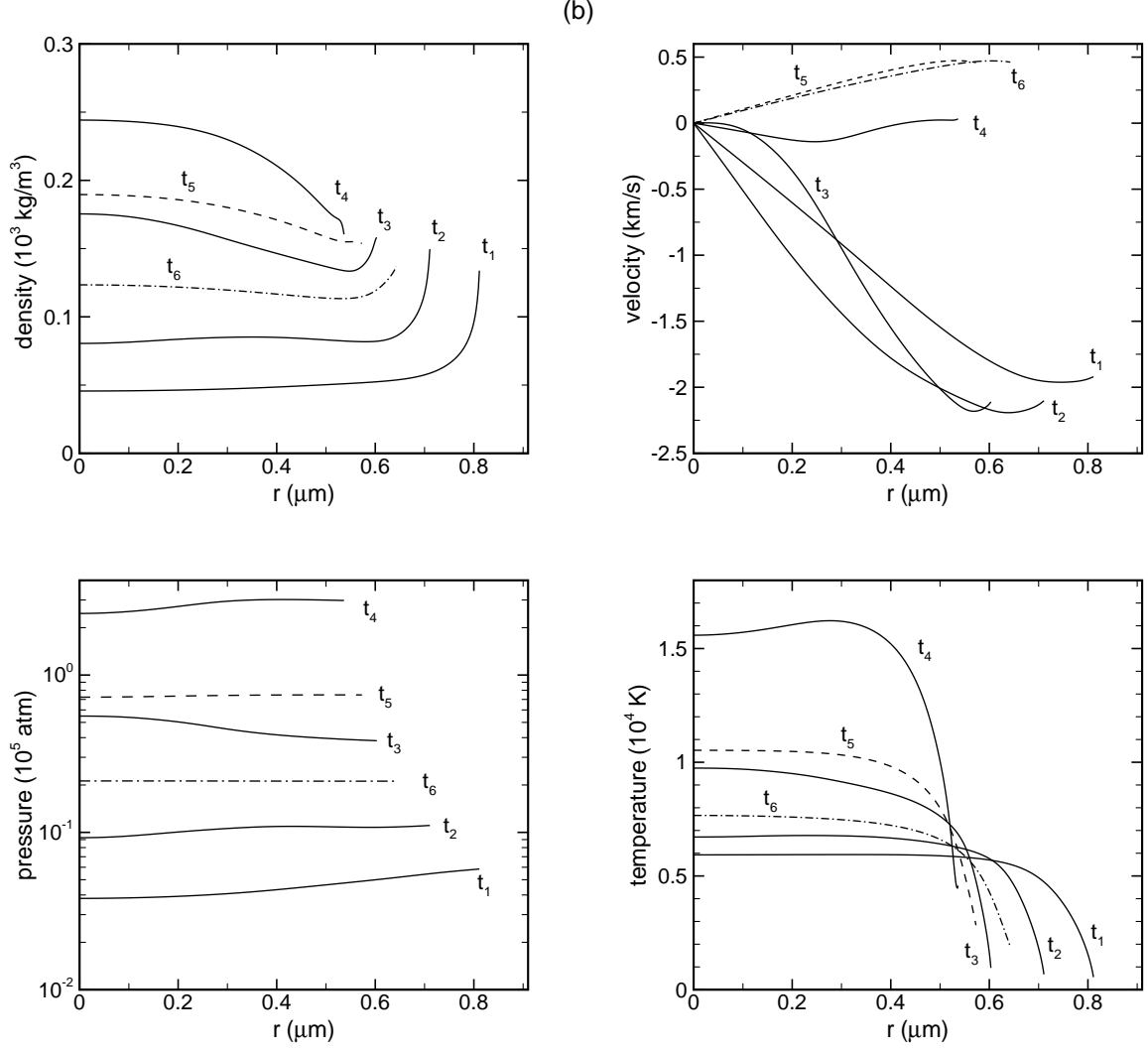


FIG. 6: Snapshots of the spatial profiles of density, velocity, pressure and temperature for $P_a = 1.35 \text{ atm}$, $R_0 = 4.5 \mu\text{m}$. (a) Xe bubble. Time sequences are $t_1 = -80 \text{ ps}$, $t_2 = -40 \text{ ps}$, $t_3 = -20 \text{ ps}$, $t_4 = 0 \text{ ps}$, $t_5 = 40 \text{ ps}$, $t_6 = 60 \text{ ps}$, where $t_4 = 0$ denotes the time of minimum radius ($t_{\min} = 22.006191 \mu\text{s}$). (b) He bubble. $t_1 = -150 \text{ ps}$, $t_2 = -100 \text{ ps}$, $t_3 = -50 \text{ ps}$, $t_4 = 0 \text{ ps}$, $t_5 = 100 \text{ ps}$, $t_6 = 250 \text{ ps}$, where $t_{\min} = 22.057459 \mu\text{s}$.

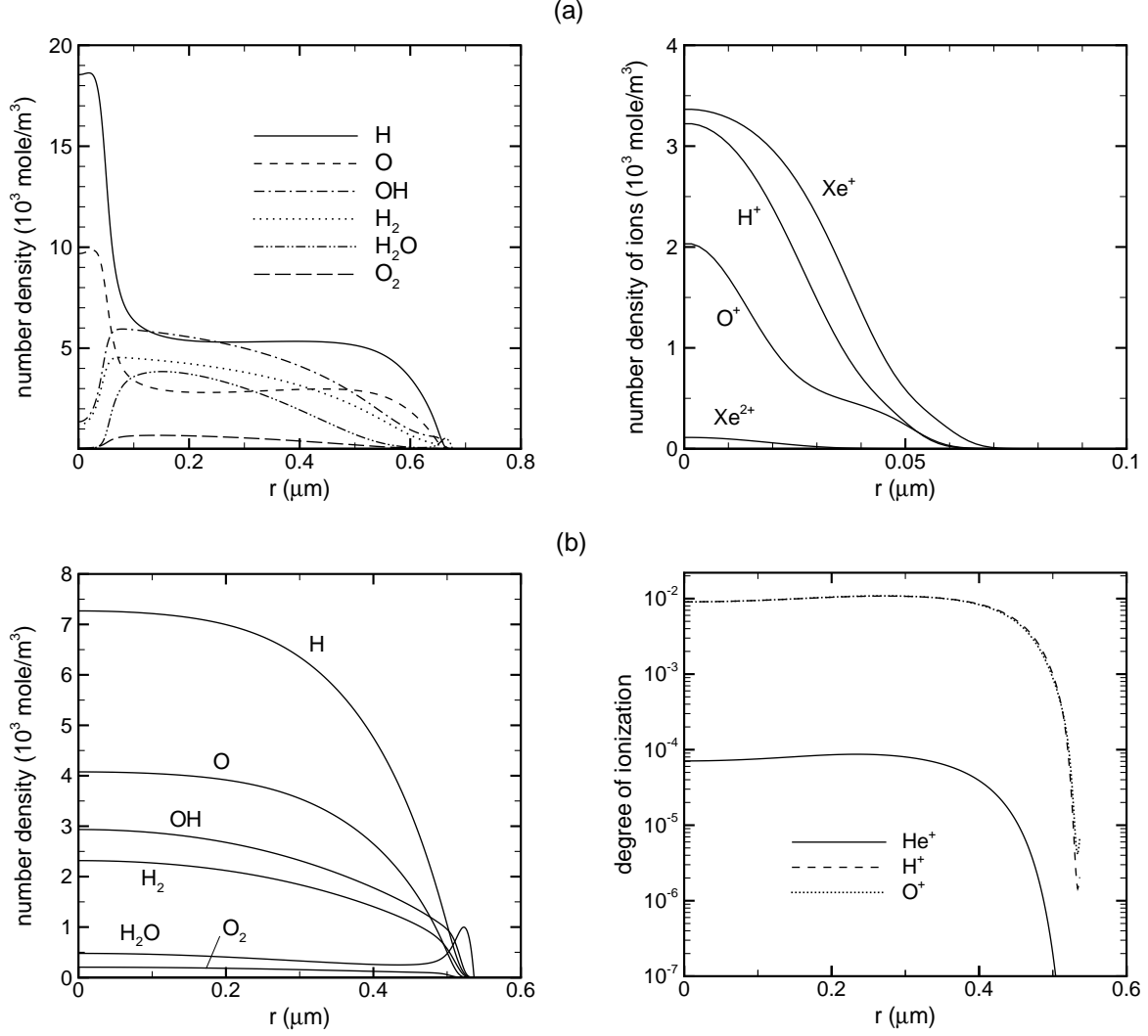


FIG. 7: The spatial profiles of the number densities of molecular species (left) and the compositions of ions (right) for $P_a = 1.35 \text{ atm}$, $R_0 = 4.5 \mu\text{m}$. (a) Xe bubble with ions computed using the nonequilibrium ionization. (b) He bubble with the degree of ionization computed using the Saha equation. All species are shown for the time of minimum radius.

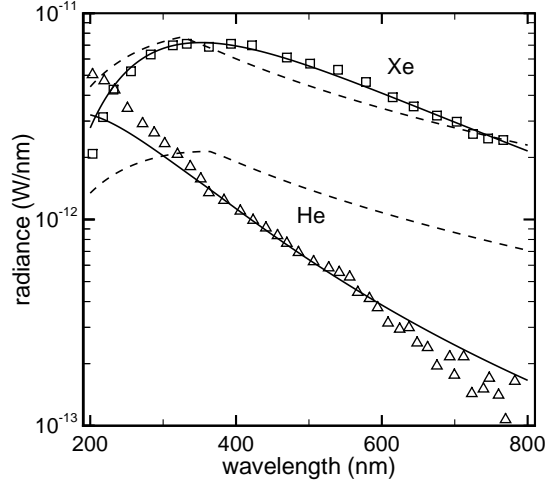


FIG. 8: Spectral radiance of the SL light from bubbles of Xe and He in water. The same parameters as in experiment [16] are Xe (the ambient radius $R_0 = 5.5 \mu\text{m}$, dissolved partial pressure 3 Torr) and He ($R_0 = 4.5 \mu\text{m}$, 150 Torr), water temperature 23°C , driving frequency 42 kHz. The squares and triangles are experimental spectra of Xe and He bubbles, respectively. The solid lines are calculated spectra of the *ad hoc* finite-size blackbody model with fitting parameters $P_a = 1.28 \text{ atm}$, $E_c = 1.80 \times 10^4$ (Xe), and $P_a = 1.45 \text{ atm}$, $E_c = 2.50 \times 10^2$ (He), and the dashed lines are those of the optically thin model with fitting parameters $P_a = 1.55 \text{ atm}$ (Xe) and 2.0 atm (He).

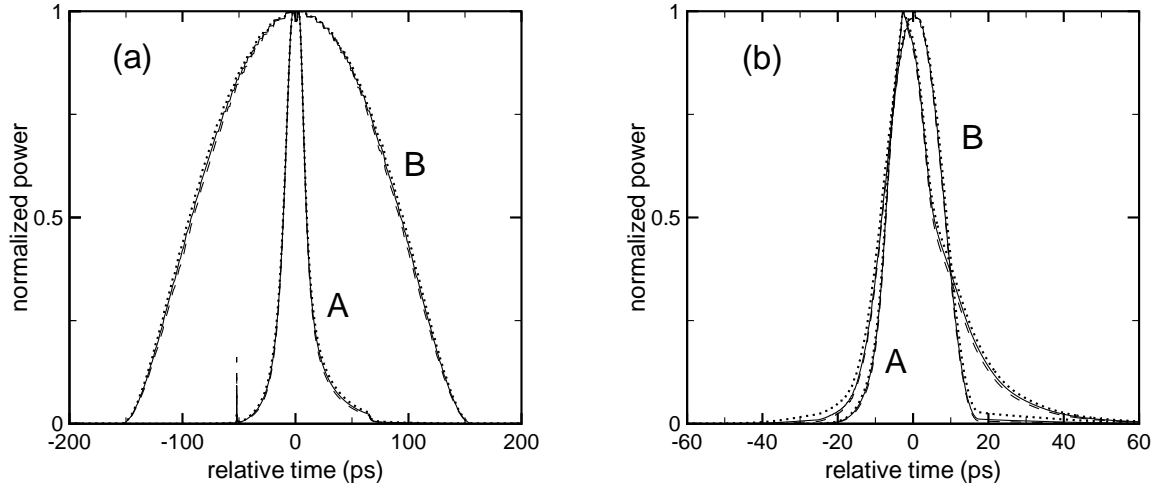


FIG. 9: Normalized radiation power vs time for the optically thin model (“A”) and the *ad hoc* finite-size blackbody model (“B”) in Xe bubble (a) and He bubble (b). The solid line denotes the total measurable power, the dashed line in the UV range ($300 \text{ nm} < \lambda < 400 \text{ nm}$), and the dotted line in the red range ($590 \text{ nm} < \lambda < 650 \text{ nm}$). Time is relative to the moment of minimum bubble radius. The parameters are the same as in Fig. 8.

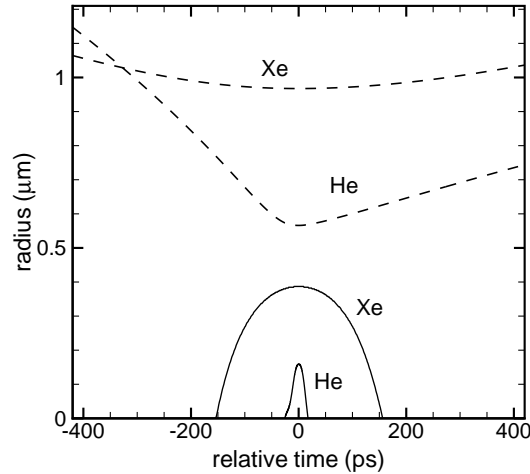


FIG. 10: The blackbody core R_c (solid line) and the bubble radius R (dashed line) vs time for Xe and He bubbles. The parameters are the same as those for the *ad hoc* finite-size blackbody model in Fig. 8.

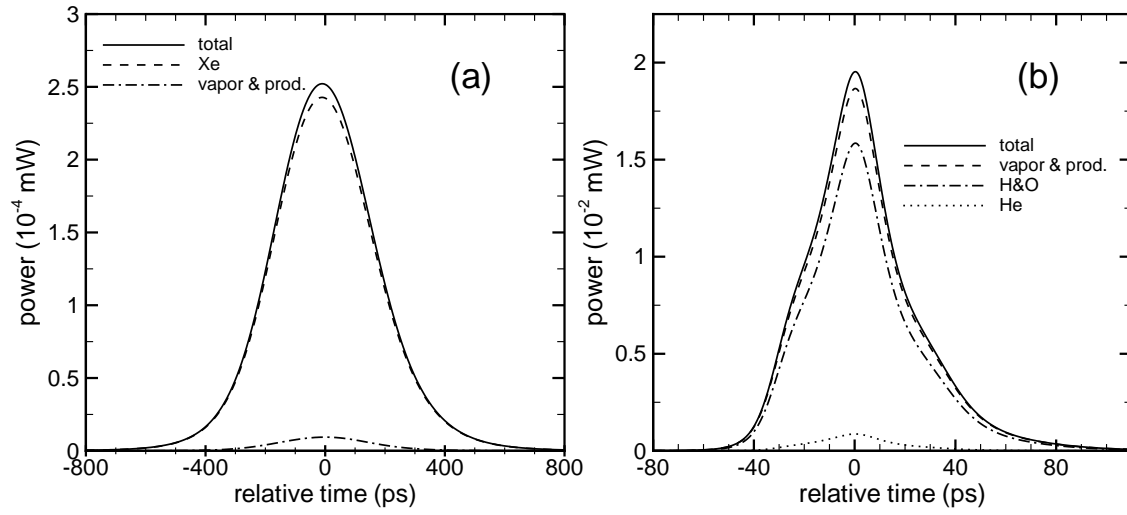


FIG. 11: The optical powers vs time for Xe (a) and He (b) bubbles computed from the optically thin model. The uppermost curve is the total power, and others are powers contributed from the species as marked. The driving pressure amplitudes are 1.28 atm for Xe bubble, and 1.45 atm for He bubble. Other parameters are the same as those in Fig. 8. Time is relative to the moment of minimum bubble radius.